Current Biology *17*, 2095–2104, December 18, 2007 DOI 10.1016/j.cub.2007.11.049

Article

The Influence of Cell Mechanics, Cell-Cell Interactions, and Proliferation on Epithelial Packing

Reza Farhadifar,[1,3] Jens-Christian Röper,[2,3] Benoit Aigouy,[2] Suzanne Eaton,[2,*] and Frank Jülicher[1,*]

[1]Max Planck Institute for the Physics of Complex Systems
Nöthnitzer Straße 38
01187 Dresden
Germany

[2]Max Planck Institute of Molecular Cell Biology and Genetics
Pfotenhauer Straße 108
01307 Dresden
Germany

Summary

Background: Epithelial junctional networks assume packing geometries characterized by different cell shapes, neighbor number distributions and areas. The development of specific packing geometries is tightly controlled; in the *Drosophila* wing epithelium, cells convert from an irregular to a hexagonal array shortly before hair formation. Packing geometry is determined by developmental mechanisms that likely control the biophysical properties of cells and their interactions.

Results: To understand how physical cellular properties and proliferation determine cell-packing geometries, we use a vertex model for the epithelial junctional network in which cell packing geometries correspond to stable and stationary network configurations. The model takes into account cell elasticity and junctional forces arising from cortical contractility and adhesion. By numerically simulating proliferation, we generate different network morphologies that depend on physical parameters. These networks differ in polygon class distribution, cell area variation, and the rate of T1 and T2 transitions during growth. Comparing theoretical results to observed cell morphologies reveals regions of parameter space where calculated network morphologies match observed ones. We independently estimate parameter values by quantifying network deformations caused by laser ablating individual cell boundaries.

Conclusions: The vertex model accounts qualitatively and quantitatively for the observed packing geometry in the wing disc and its response to perturbation by laser ablation. Epithelial packing geometry is a consequence of both physical cellular properties and the disordering influence of proliferation. The occurrence of T2 transitions during network growth suggests that elimination of cells from the proliferating disc epithelium may be the result of junctional force balances.

*Correspondence: eaton@mpi-cbg.de (S.E.), julicher@pks.mpg.de (F.J.)

[3]These authors contributed equally to this work.

Introduction

The capacity of epithelial cells to modulate intercellular junctional contacts is essential for tissue form and function. Junction remodeling underlies many of the dramatic tissue reorganizations occurring during development, including convergent extension and invagination [1–6]. Epithelial rearrangements also allow the development of specific packing geometries. Hexagonal packing in the vertebrate lens minimizes light scattering by plasma membranes [7]. Hexagonally packed hairs on the surface of the *Drosophila* wing guide airflow during flight [8]; their packing reflects the underlying hexagonal organization of pupal-wing epithelial cells. However, these cells are irregularly packed throughout most of wing development. Remodeling of epithelial contacts to form a hexagonal array occurs shortly before hair formation [9].

Much is known about the molecular machinery that reorganizes epithelial contacts. The epithelial zonula adherens contains many proteins with both adhesive and contractile functions. The homophilic adhesion molecule E-cadherin not only mediates adhesion between adjacent cells but also organizes a subcortical actin-myosin cytoskeleton. Increased E-cadherin trafficking is essential for junction remodeling in the wing [9]. Modulation of actin-myosin contractility can alter the morphology of the junctional network and is thought to contribute to morphogenetic movements in epithelial sheets [3, 10, 11]. We expect that these molecules alter cell packing by changing force balances within the epithelium. To understand remodeling, one must develop a physical description of the epithelium that can account for rearrangements of the junctional network.

Here, we investigate the physical basis of epithelial cell packing in the third instar larval wing disc of *Drosophila.* During larval stages, this tissue proliferates rapidly, increasing from approximately 40 to greater than 50,000 cells. The geometric disorder induced by cell division in proliferating epithelia was first studied in 1928, when F.T. Lewis examined the epidermal cells of the cucumber [12]. Lewis noted that cells with different neighbor numbers were present in reproducible proportions, and their average areas varied linearly with neighbor number. Although less than half the cells were hexagonal, the average neighbor number was near six. The statistics of neighbor numbers in proliferating tissues were recently discussed by Gibson et al. [13], who argued that the fraction of n sided polygons in the junctional network can be determined by simple topological rules describing allocation of neighbors after cell division. These topological rules are not based on the physical properties of the cells. However, we expect the redistribution of neighbors after cell division to depend on physical cellular properties. Also, a purely topological description cannot account for cell size and shape or local force balances.

In order to describe packing geometries at apical junctions on the basis of the physical properties of

Box 1. Physical Description of Cell Packing in Epithelia

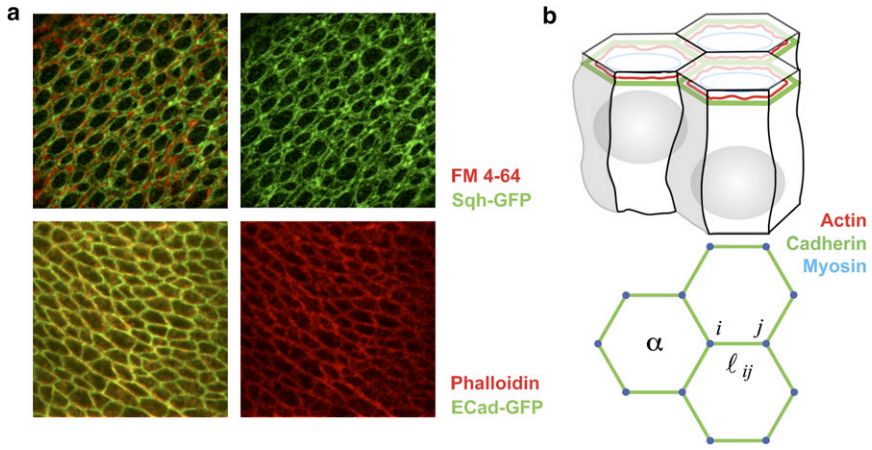

Figure A. Adhesion and Contractility at Apical Junctions

Epithelia are composed of a sheet of cells of similar height that are connected via cell-cell adhesion. The adhesion molecule Cadherin and components of the actin cytoskeleton are enriched apicolaterally (Figure A_a). Cell packing geometry can be defined by the network of adherens junctions (Figure A_b). This network is described by a vertex model with N_C polygonal cells numbered by $\alpha = 1 \ldots N_C$ and N_V vertices, numbered $i = 1 \ldots N_V$ at which cell edges meet. Stationary and stable network configurations satisfy a mechanical force balance; this implies that at each vertex, the total force $\boldsymbol{F}_i$ vanishes. We describe these force balances as local minima of an energy function

$$E(\boldsymbol{R}_i) = \sum_{\alpha} \frac{K_\alpha}{2}\left(A_\alpha - A_\alpha^{(0)}\right)^2 + \sum_{<i,j>} \Lambda_{ij}\ell_{ij} + \sum_{\alpha} \frac{\Gamma_\alpha}{2} L_\alpha^2$$

for which $\boldsymbol{F}_i = -\dfrac{\partial E}{\partial \boldsymbol{R}_i}$.

The energy function describes forces due to cell elasticity, actin-myosin bundles, and adhesion molecules. The first term describes an area elasticity with elastic coefficients K_α, for which A_α is the area of cell α and $A_\alpha^{(0)}$ is the preferred area, which is determined by cell height and cell volume. The second term describes line tensions Λ_{ij} at junctions between individual cells. Here, ℓ_{ij} denotes the length of the junction linking vertices i and j and the sum over $<ij>$ is over all bonds. Line tensions can be reduced by increasing cell-cell adhesion or reducing actin-myosin contractility. The third term describes the contractility of the cell perimeter L_α by a coefficient Γ_α, which could reflect, for example, the mechanics and contractility of the actin-myosin ring (Figure A_a).

epithelial cells, we develop a 2D network model that describes forces that act to displace vertices. Cell packings correspond to stable and stationary network configurations obtained by minimization of a potential function. We use this approach to study the role of cell mechanics and cell division in determining network packing geometry. We compare our results to the proliferating larval wing epithelium of *Drosophila* and estimate the parameters characterizing the effects of contractility and adhesion in this tissue. We independently estimate parameter values by analyzing movements of the junctional network after laser ablation of individual cell boundaries and comparing them to the corresponding behaviors in our model.

Results

Physical Description of Cell Packing: A Vertex Model

Apical junctions can be considered as a 2D network that defines the cell packing geometry. By using a vertex model, we describe the packing geometry of the junctional network (Box 1). Cells are represented as polygons with cell edges defined as straight lines connecting vertices—a good approximation for the wing disc epithelium. Junctional-network configurations that are stable on timescales shorter than those of cell division correspond to those network configurations in our model for which the packing geometry is stable and stationary. These configurations obey a force balance, which implies that the net force $\boldsymbol{F}_i$ (Box 1) acting on each vertex vanishes for all vertices. In general, forces acting on the junctional network need not be forces derived from an energy. However, the forces we consider here can in our simple description be represented by the energy function $E(\boldsymbol{R}_i)$ presented in Box 1. Any stable and stationary configuration of the network then corresponds to a local minimum of the energy function. This provides a framework for calculating stable cellular packing geometries. Similar energy functions have been used in previous works [14–16]. Our vertex model is different in that we represent only the network of apical junctions, and we introduce a quadratic perimeter energy.

We consider three contributions to the potential energy $E(\boldsymbol{R}_i)$ of a particular configuration of the epithelial junctional network given in Box 1: area elasticity, line tension along apical junctions, and contractility.

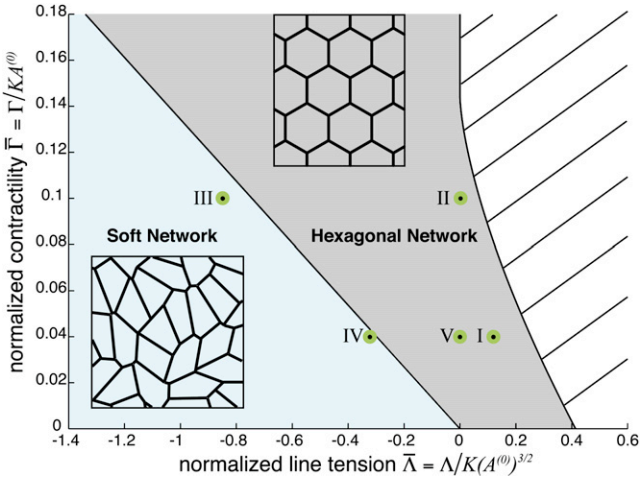

Figure 1. Ground-State Diagram of the Vertex Model

Diagram of the ground states of the energy function $E(R_i)$ as a function of the normalized line tension $\overline{\Lambda}$ and contractility $\overline{\Gamma}$. In the gray region, the ground state is a hexagonal network as indicated. In the blue region, the ground states are irregular soft networks (an example corresponding to case III is shown), and many configurations coexist. In the striped region to the right, where $\overline{\Lambda}$ is large, cell areas vanish and the model breaks down. Green dots indicate parameter values of five different cases (case I: $\overline{\Lambda} = 0.12$, $\overline{\Gamma} = 0.04$; case II: $\overline{\Lambda} = 0$, $\overline{\Gamma} = 0.1$; case III: $\overline{\Lambda} = -0.85$, $\overline{\Gamma} = 0.1$; case IV: $\overline{\Lambda} = -0.32$, $\overline{\Gamma} = 0.04$; and case V: $\overline{\Lambda} = 0$, $\overline{\Gamma} = 0.04$).

Although our 2D description does not explicitly take into account cell height, area elasticity does so indirectly. Assuming that cell volume stays constant, altering the cross-sectional area of a cell at the junctional level involves a deformation of the cell in three dimensions. Whereas the model describes single cells as elastic objects, the cellular network is plastic because the model takes into account junction remodeling (see below).

Line tension Λ_{ij} (Box 1) describes forces resulting from cell-cell interactions along the junctional regions of specific cell boundaries. Multiple mechanisms might influence line tension, which could vary from edge to edge. For example, adhesive interactions between cells could favor cell-boundary expansion, whereas the subcortical actin cytoskeleton might oppose it. As the length of the cell boundary ℓ_{ij} between two vertices *i* and *j* increases, this term in the energy function decreases if the line tension Λ_{ij} is negative and increases if Λ_{ij} is positive. In addition to the subcortical actin cytoskeleton, many epithelial cells assemble an actin-myosin belt that underlies the cortex at the level of apical junctions (Figure A_b). Because actin-myosin contractility would tend to reduce the perimeter of each cell, it not only contributes to the line tension but is also expected to generate the coefficient Γ_α, describing the dependence of contractile tension on cell perimeter L_α (Box 1). This contractility term involves the whole cell perimeter and is motivated by the fact that the actin-myosin ring appears to span the entire cell.

Before studying tissue morphologies, we first discuss some general properties of the model. An important feature is the ground state, or the most relaxed network configuration. As discussed below, these ground states do not correspond to realistic tissue morphologies; however, ground states are important reference states. For a situation when all cells are identical, $A_\alpha^{(0)} = A^{(0)}$, $K_\alpha = K$, $\Gamma_\alpha = \Gamma$ for all cells, and $\Lambda_{ij} = \Lambda$ for all edges. Figure 1 shows that two main types of ground states exist as a function of the model parameters. The geometry of the ground state is determined by the two normalized parameters $\overline{\Gamma} = \Gamma/K A^{(0)}$ and $\overline{\Lambda} = \Lambda/K(A^{(0)})^{3/2}$. Here, $\overline{\Gamma}$ is a normalized contractility; when small, it implies that contractile forces are small compared to those from area elasticity. Similarly, $\overline{\Lambda}$ is a line tension, normalized to area elastic tensions. When it is negative, cell boundaries tend to expand; when it is positive, they tend to shrink.

Two regions exist in the ground-state diagram shown in Figure 1. In the gray region, regular hexagonal packing geometry is the single ground state. This network configuration has both a bulk modulus and a shear modulus—i.e., work is required to compress or expand the tissue and also to shear it. In the blue region, the ground state is degenerate, i.e., there exist many packing geometries all with the same minimal energy. They share the common feature that the area of all cells is equal to the preferred area $A^{(0)}$, and their perimeters are equal to $L_0 = -\Lambda/2\Gamma$. As a consequence of this degeneracy, the configuration can be sheared without any work required. The system is soft with vanishing shear modulus and behaves more like a liquid in which cells can move past one another easily. We call this state a soft network. Whereas the hexagonal ground state in the gray region is regular, the soft network ground states are typically irregular. Examples of configurations corresponding to points III and IV are shown. Analysis of the ground states reveals that the morphologies and material properties of junctional-network configurations depend strongly on the model parameters and that there exists a phase transition between a solid and a soft state.

Packing Irregularity Induced by Cell Division

In addition to the global energy minimum or ground state, there exists for any choice of parameters an even larger number of local energy minima, which all could represent stable cell packing geometries. We think of a developing epithelium as assuming a sequence of stable network configurations, which undergo rearrangements in response to local perturbations that affect the stable configuration. Such perturbations include cell division and apoptosis but might also correspond to slow changes in cellular properties. This quasistatic approximation allows us to define a history of stable configurations by slowly and locally modifying model parameters. Thus, a particular packing geometry is the consequence of the history of such perturbations.

By using our model, we can numerically simulate the evolution of cell packing geometry during tissue growth. We randomly select one cell and divide it by the following algorithm: We doubled the preferred area of the cell

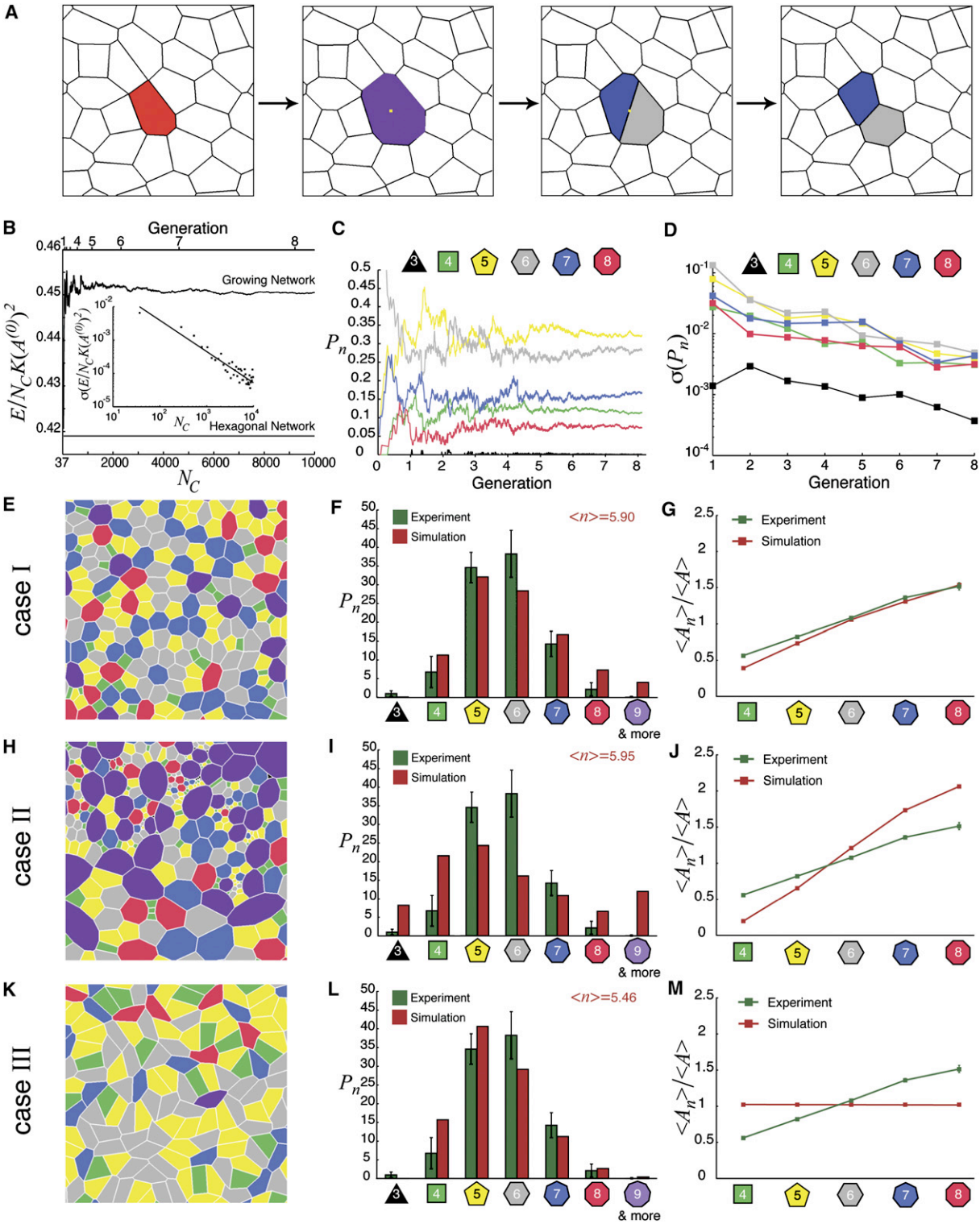

Figure 2. Cell Division, Topology, and Morphology

(A) Cell division in the vertex model. The preferred area of a randomly chosen cell is increased, and the network is relaxed. A new cell boundary is introduced with a random orientation. Both new cells are assigned the initial preferred area, and the resulting network is again relaxed. The yellow dot indicates the average vertex position of the original cell through which the new boundary is initially formed.

(B) Normalized energy per cell of a growing network as a function of the number N_C of cells for parameter values corresponding to case I (see Figure 1 and Box 1). Generation number is also indicated. The energy approaches a value that is greater than the ground-state value of the hexagonal network. The standard deviation, averaged over 250 individual divisions, is indicated as a function of cell number in the inset.

(C) Fraction P_n of cells with n neighbors as a function of generation number in a growing network for case I.

(D) Logarithmic plot of standard deviation of P_n as a function of generation number for the simulation of case I. The slope of the lines represents the characteristic generation number, at which the standard deviation decreases 10-fold.

quasistatically with a conjugate gradient method (see Supplemental Experimental Procedures available online) to determine and follow the sequence of local energy minima as the preferred area $A_\alpha^{(0)}$ is increased in small steps (Figure 2A, first and second panels). After its size is doubled, we divide the cell by introducing vertices generated by a new edge that is formed at a random angle and that passes through the cell center, defined as the average of the vertex positions of the original cell (Figure 2A, third panel). The two daughter cells that are created by this procedure are assigned the parameters of the other cells, including the preferred area $A^{(0)}$. The resulting configuration is then again relaxed to the nearest stable state (Figure 2A, fourth panel). During this relaxation, edges might shrink or vanish if this leads to a further lowering of the energy. This can be followed by a T1 transition during which a new edge expands and the topology of the network is changed (Figure S1A). If, during the relaxation, the area of a cell drops to zero, the cell is eliminated by a T2 process (Figure S1B). T1 and T2 processes describe topological changes of cellular networks. They have been introduced in the context of foam physics [17].

Starting with a hexagonal lattice of 36 cells, we simulate proliferation by repeating this algorithm. Simulation results for $\overline{\Gamma} = 0.04$ and $\overline{\Lambda} = 0.12$ (case I) are shown in Figures 2B–2G (see also Movie S1). The energy per cell first increases with increasing cell number and then fluctuates around a constant value that is larger than the ground-state value of the hexagonal lattice (Figure 2B). During this process, a distinct network pattern emerges that is characterized by the fraction P_n of cells of different polygon classes (i.e., cells with different numbers of neighbors, n) and by the average areas A_n of n-sided cells. For increasing numbers of cell, the fraction P_n of n-sided cells (Figure 2C), and their average area A_n (Figure S2D, case I) converge to constant values. The standard deviations $\sigma(P_n)$ and $\sigma(A_n)$ of both the fraction and the area of n-sided cells decrease exponentially with characteristic generation numbers 3.14 and 3.60, respectively (Figure 2D and Figure S2E, case I). Beyond the larger of these characteristic generation numbers, the tissue patterns become stationary for increasing generation number. After simulating approximately eight generations of cell division (from 36 to 10,000 cells), the standard deviations $\sigma(P_n)$ and $\sigma(A_n)$ are less than 1% (Figure 2D and Figure S2E, case I). A representative network illustrating this stationary state is shown in Figure 2E, and the corresponding steady-state values of P_n and A_n for different polygon classes are shown in Figure 2F (red bars) and Figure 2G (red lines). For this network, pentagons are the most frequent polygon class, and the average neighbor number is 5.90. This implies that 2.44% fourfold vertices exist. The average area A_n increases for increasing n as shown in Figure 2G.

In order to study how tissue morphology is influenced by the physical properties of cells, we performed simulations by systematically varying parameter values. In addition to case I, results from two parameter sets corresponding to cases II and III (Figure 1) are presented in Figures 2H–2M and Figure S2 (see also Movies S2 and S3). In case II ($\overline{\Gamma} = 0.1$, $\overline{\Lambda} = 0.0$), contractility is large relative to area elasticity, and the ground state is a hexagonal network as it is in case I. For case III ($\overline{\Gamma} = 0.1$, $\overline{\Lambda} = -0.85$), line tension is negative, and the ground state corresponds to a soft network (see Figure 1). As in case I described above, the fractions P_n and average areas A_n of polygon classes converge during growth simulations for cases II and III (Figures S2C–S2E). The resulting network morphologies, however, differ dramatically (Figures 2E, 2H, and 2K). In case II (Figure 2H), the stationary network contains a smaller fraction of hexagonal cells than case I (Figure 2I, red bars, and Table S1). Pentagons are most common; however, there is also a much larger fraction of cells with nine or more sides (Figure 2I, red bars)—even 20 sided polygons occur. The average areas A_n also vary more strongly with neighbor number than in case I (Figure 2J, red line). As in case I, the energy per cell first increases with increasing cell number and then converges to a stationary value that is larger than that of the hexagonal ground state (Figure S2A, case II).

In case III, the coefficients $\overline{\Gamma}$ and $\overline{\Lambda}$ are such that the ground state is a soft network (Figure 1). Under these conditions, simulating proliferation generates the stationary network morphology shown in Figure 2K. Pentagons are the most common polygon class, and the average neighbor number is smaller than in case I (Figure 2L, red bars, and Table S1). Unlike cases I and II, the energy does not increase when cells are divided (Figure S2A, case III); the irregular morphology shown in Figure 2K is a ground state of the energy; all polygons have the same area $A^{(0)}$ and the same perimeter $L_0 = -\Lambda/2\Gamma$. As a consequence, the cell area does not depend on neighbor number (Figure 2M, red line). Finally, the rate of T1 and T2 transitions occurring during growth depends on parameters and differs markedly in cases I–III (Table S1). Simulations performed with two additional parameter sets (cases IV and V in Figure 1) are shown in Figure S3.

These results show that cell proliferation can generate packing disorder with specific reproducible features that depend on the physical properties of the cells as described by the parameters $\overline{\Gamma}$ and $\overline{\Lambda}$. This suggests that we can obtain information about parameter values from quantitative analysis of cellular packing in proliferating epithelia. To quantitatively describe cell packing geometry in the wing disc, we analyzed 1738 cells from different confocal images of living wing discs expressing E-cadherin-GFP by using an automated image-processing algorithm to outline the network of

(E, H, and K) Examples of stationary network patterns generated by repeated cell division for cases I, II, and III. Color code for polygon class is the same as that used in (F), (I), and (L).

(F, I, and L) Stationary distributions of neighbor numbers P_n for cases I, II, and III (red bars). The average neighbor number is indicated. The green bars in each panel indicate the same experimentally determined distribution of neighbor numbers in the third instar wing imaginal disc, for comparison.

(G, J, and M) Average areas of different polygon classes normalized to the average area of cells in the network, $\langle A_n \rangle / \langle A \rangle$, for cases I, II, and III (red lines). These lines are compared to the experimentally determined values for the third instar wing disc (green lines).

apical junctions (Supplemental Experimental Procedures and Figures S1A–S1D). From this network, we identify individual cells, cell boundaries, and three- and four-fold vertices. We define a four-fold vertex as a region of contact between four cells, the size of which does not exceed the average width of cell boundaries in the image. This cutoff corresponds to 2 pixels—approximately 20% of the average cell-boundary length. We use this information to determine the fraction of cells with different numbers of neighbors (Figures 2F, 2I, and 2L, green bars) and the average areas of cells within different polygon classes (Figures 2G, 2J, and 2M, green lines). These data are shown repeatedly alongside the values obtained by simulations in cases I, II, and III. The distribution of polygon classes we observe is in good agreement with previous results [9] and differ slightly from those of [13]. This probably reflects the different methods used for assigning cells to polygon classes. Polygon-class distribution depends on the cutoff used to distinguish boundaries from four-way vertices (Figure S4D). In the wing disc, average cell areas increase with neighbor number (Figures 2G, 2J, and 2M, green lines). The average area of hexagonal cells is slightly larger than the average area of cells in the epithelium (108%). The average area of five-sided cells is 82% of the average area of all cells and that of seven-sided cells is 136% (Table S1).

Packing geometry and area variation of the disc epithelium are clearly different from those obtained by simulations in cases II and III. In case III, cell areas do not vary at all with neighbor number, unlike those of real tissue. Case II gives a much broader distribution of polygon classes than that of the disc epithelium, and average areas vary more strongly with side number. Of the three conditions discussed, case I produces morphologies closest to that of real tissue. Furthermore, we estimate the rate of T2 transitions during imaginal disc growth to be 10 ± 2 per 100 cell divisions (see Supplemental Experimental Procedures and Figure S4E). This value is most consistent with case I (12/100 cell divisions) and differs markedly from cases II and III (Table S2). Performing simulations, systematically varying parameters, shows that only a limited set of values of $\overline{\Gamma}$ and $\overline{\Lambda}$ generates neighbor-number distributions (Figure 3, red region) and area variations (Figure 3, blue region) similar to those of the larval wing epithelium. The overlap of these regions includes the parameter values used in case I. Within this region of overlap, the ground-state packing geometry is hexagonal (Figure 1). Thus, proliferation produces a disordered packing that represents a local energy minimum rather than a globally relaxed state.

Probing Mechanical Properties of the Junctional Network by Laser Ablation

The vertex model describes steady-state force balances. To investigate the interplay of forces acting at the junctional network of disc epithelial cells, we perturb the stable network by ablating a section of individual cell boundaries with a UV laser beam focused on a spot of 1.3 μm diameter in the plane of epithelial junctions (see Supplemental Experimental Procedures). A single-cell boundary was cut, and the resulting movements of the network, visualized with E-cadherin-GFP, were observed over several minutes (Figures 4A–4C and 4E and Movie S4). In response to the cut, E-cadherin-GFP fluorescence disappeared from the center of the cut cell boundary, and the vertices at both ends moved from their initial positions, thereby increasing their distance from the cut point. Subsequently, they relaxed to new stable positions. In most cases (20/24), the distance d between the vertices increased as $d = d_0 + d_1 - d_1\exp(-t/\tau)$ for which $d_0 + d_1$ is the final distance and d_0 is the initial distance (Figure 4D, black points). The relaxation time τ varied between 13 and 94 s. Wound healing, in which neighboring cells actively and specifically extrude the two cut cells, occurred over much longer time scales (~20 min; Movie S5). Occasionally (4/24), more complex movements were observed; however, the final distance between the two vertices was always larger than the initial distance (Figure S5). The initial extension of the cut bond upon ablation suggests that cell boundaries are under tension and that $\overline{\Lambda}$ is positive.

To determine whether the displacements after laser ablation depended on actin-myosin contractility, we treated imaginal discs with the Rho-kinase inhibitor Y-27632 [18] and quantified movements occurring upon laser ablation. Rho-kinase-mediated phosphorylation of myosin light chain (Spaghetti Squash) is required for myosin activity [19]. The average magnitude of displacements was significantly reduced upon drug treatment (Figure 4D, blue points), indicating that tension at cell boundaries depends on actin-myosin contractility.

To examine how the junctional network relaxed in response to laser ablation, we measured displacement vectors $\boldsymbol{D}$ of vertices in the field of cells surrounding the cut point. The average displacement vectors at different angles and different distances are shown in Figure 4F. A more detailed description of vertex displacements is available in the Supplemental Experimental Procedures (Figures S6 and S7). The displacement field is anisotropic, and movements occur mainly along the direction of the cut boundary. In the direction perpendicular to the cut boundary, small inward movements occur (Figure 4F).

In order to quantify the local anisotropy of displacements near the cut bond, we determined the area and perimeter changes of the two cells adjacent to the cut bond after the two adjacent vertices had reached their new stable positions. Laser ablation might affect both localized line tensions and general contractility of the cut cells. Removing contractility would be expected to result in isotropic expansion, whereas removing local bond tension is expected to produce more anisotropic deformations. In the idealized case of a completely isotropic deformation, perimeter would increase linearly with the increase in length of the cut bond (Figure 5A). In contrast, a strongly anisotropic deformation would result in little or no change in the perimeter (Figure 5B). Real deformations might comprise a superposition of both anisotropic and isotropic movements. In experiments, perimeter changes only slightly as a function of the bond length increase, and area changes roughly linearly (red points in Figures 5C and 5D), thus reflecting a strong anisotropic component of the deformations.

The measurements of changes ΔA_{cut} and ΔL_{cut} in the combined area and perimeter of the two cells adjacent

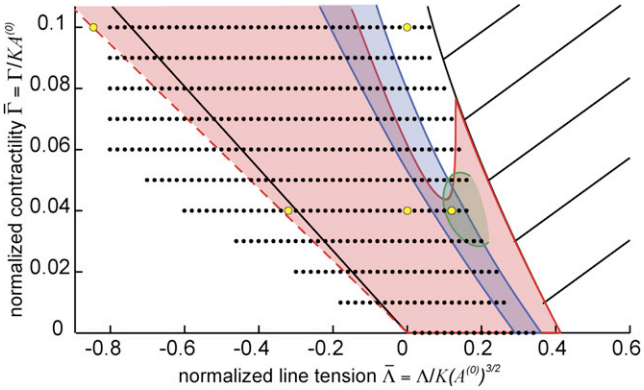

Figure 3. Parameter Regions Matching Observed Tissue Properties

Properties of cell packing for different values of the parameters $\overline{\Lambda}$ and $\overline{\Gamma}$ line tension and contractility; K is the area elastic coefficient and $A^{(0)}$ is the preferred area of cells. Simulations of tissue growth were performed for different parameter values (black dots). In the red outlined region, the distribution P_n of n sided cells in simulations is similar to the one observed in the wing disk of *Drosophila* ($\Delta_P < 0.004$, see Supplemental Experimental Procedures). In the blue outlined region, the relative areas of n sided cells match those observed in experiments ($\Delta_A < 0.07$). Comparing simulations of laser ablation with experiments, we find quantitative agreement in the green outlined region ($\Delta_L < 0.07$). Yellow dots indicate cases I–V. The straight solid line indicates the transition between the soft lattice and the hexagonal ground state. It is not possible to simulate proliferation to the left of the dashed red line with our current proliferation algorithm. The hatched region corresponds to that shown in Figure 1.

to the cut boundary can be compared to those obtained in simulations for estimating parameter values of the vertex model. In the vertex model, we can study the displacements that follow the removal of individual bonds in a stable and stationary network configuration. We can thus mimic bond-cutting experiments starting from a stable network morphology generated by the growth algorithm described in the last section. To simulate laser ablation, we randomly select bonds for removal. We set to zero the normalized line tension $\overline{\Lambda}_{ij}$ of the cut bond as well as the normalized contractility $\overline{\Gamma}_{\alpha}$ of the cells sharing the cut bond. Removal of both these terms is necessary for achieving quantitative agreement between simulations and experiments (see Supplemental Experimental Procedures). We then numerically determine the new relaxed network configuration after these local parameter changes by using the conjugate gradient method described previously. For a given pair of parameters $\overline{\Gamma}$ and $\overline{\Lambda}$ for all other cells, we determine the resulting distributions of area and perimeter changes of the pair of cells sharing the removed bonds. The gray points in Figures 5C and 5D show normalized area and perimeter changes, with respect to the normalized change in bond length, for many different removed bonds in the case that $\overline{\Lambda} = 0.12$ and $\overline{\Gamma} = 0.04$ for cells surrounding the cut cells (case I). Here, experiment and theory match quantitatively. As we move away from the parameter values of case I, the calculations and experiment begin to differ (for example Figures 5E and 5F). From these calculations, we conclude that there is a small parameter region near case I (outlined in green in Figure 3) where theory matches the experiments. Simulations with these parameters also accurately describe the displacement of vertices in the field of cells surrounding the cut bond (Supplemental Data and Figures S6 and S7).

By performing simulations of both proliferation and laser ablation, we have been able to estimate the relative magnitude of the coefficients describing cell elasticity, contractility, and line tension in the wing disc. These data show that line tension Λ on individual cell boundaries is positive (i.e., contractility predominates over adhesive cell-cell interactions at cell boundaries). Furthermore, we find that a general contractility described by the perimeter elasticity Γ is also required to account for our experimental observations. A perfect hexagonal lattice represents a global minimum of the energy function for epithelia with these physical properties; the disordered packing geometry induced by proliferation reflects a local minimum with a higher value of the energy function.

Discussion

Many genes that play a role in epithelial junction remodeling have been identified [3, 9, 20]. Their gene products influence physical cellular properties; this in turn triggers cellular rearrangements. However, the physical mechanisms involved in rearrangement of epithelial cell packing are not understood. Here, we describe and quantify for the first time the force balances in the apical junctional network of an epithelium: the proliferating wing disc epithelium of *Drosophila.* We combine experiment and theory to understand how the physical properties of these cells influence cell packing geometry and morphology.

To investigate the contributions of cell mechanics, adhesion, and cortical contractility to the development of specific packing geometries, we have developed a vertex model for the junctional network. Configurations of the junctional network observed in tissues correspond to network configurations for which forces are balanced. Two different types of relaxed network configurations, corresponding to global minima of an energy function, occur: a solid-like hexagonal network and a liquid-like soft network, which is irregular (Figure 1). Because of its liquid nature, this state of the network can be easily remodeled. This suggests that increased adhesion (leading to negative boundary tension) might in some instances actually facilitate rearrangement—it will be interesting to investigate whether such a situation occurs in vivo, for example during convergent extension.

Packing geometries observed in vivo correspond in our vertex model to local minima of an energy function. We have shown that irregular tissue morphologies in the wing disc can be accounted for by changes introduced by proliferation. We have simulated network

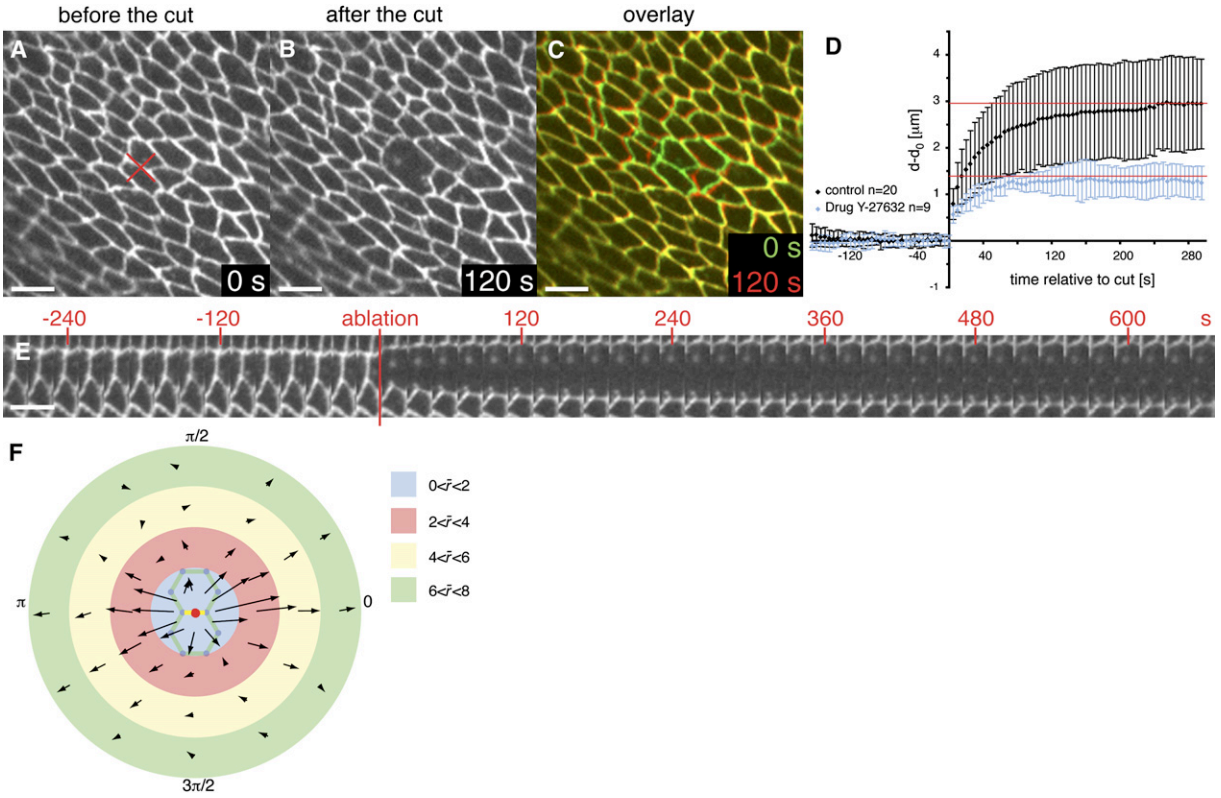

Figure 4. Laser-Ablation Experiments

(A and B) Single confocal images of a GFP-E-cadherin-expressing wing disc during a laser-ablation experiment. (A) shows the epithelial network before the cut, and (B) shows the same network 120 s after the cut. The red cross in (A) indicates site of ablation.

(C) Overlay of images (A) in green and (B) in red. Ablations focused on more basolateral regions of the cell boundaries, below the junctional region, did not result in significant displacements (not shown).

(D) Change in distance $d - d_0$ between vertices at the ends of the ablated bond as a function of time, averaged over 20 experiments. The initial bond length is denoted d_0. Error bars represent SDs. Blue points show displacements in Y-27632 treated discs. Black points show displacements in untreated discs. Red lines indicate calculated maximum bond-length change d_1. For untreated discs, $d_1 = 2.85$ μm. For Y-27632 treated discs, $d_1 = 1.41$ μm.

(E) A sequence of cropped images of the ablated region, separated by 20 s. The time in seconds is indicated. Scale bars represent 5 μm in (A)–(C) and (E).

(F) Average displacement vectors (black arrows) at different angles and different distances from the cut boundary (yellow line, center). Distance from the cut site (red dot) is color coded as indicated.

morphologies in growing tissues and studied neighbor numbers as well as area variations of cells for different values of parameters describing cellular physical properties. In our simulations of proliferation, the network morphology converges to a steady state that depends on the parameter values. Only a subset of parameter choices is consistent with the cell shapes and network morphologies observed in the proliferating wing disc. In other parameter ranges, different network types occur (Figure 2 and Figure S3). There is a broad region of parameter values for which good agreement with observed neighbor numbers exists (red outlined region in Figure 3). Recent work based on topological arguments has shown that proliferation leads to stationary neighbor-number distributions after only a few rounds of cell division. The distribution of neighbor numbers depended on simple rules for neighbor reallocation [13]. Our work shows that neighbor reallocation after cell division depends on cellular physical properties.

In simulations of cases I–V, we find that the average areas of n-sided polygons approximately shows a linear relationship between side number and average area, $\langle A_n \rangle / \langle A \rangle \approx 1 + \lambda(n-6)$, in which the coefficient λ depends on model parameters (Figures 2G, 2J, and 2M). This relation has been termed Lewis's law [21]. It can be shown that cellular networks with this property are dominant in the plane's random polygonal tilings that are subject to the constraints of space filling and an average neighbor number of 6. Of the cases I–III, only in case I is the value of λ close to the one observed in the wing disc (Figure 2G). More generally, area variations observed experimentally are in good agreement with simulations for parameter values within the blue outlined region (Figure 3).

We have performed laser-ablation experiments of cell boundaries to study the force balances described by our vertex model and to independently determine parameter values. Laser-induced cutting of cell junctions causes the vertices at either end to move apart. This results in anisotropic displacements of vertices in the surrounding network; displacements are maximal for those vertices lying along the axis of the cut bond. Comparing these experiments to simulations shows that only a small range of parameters (green outlined region of Figure 3),

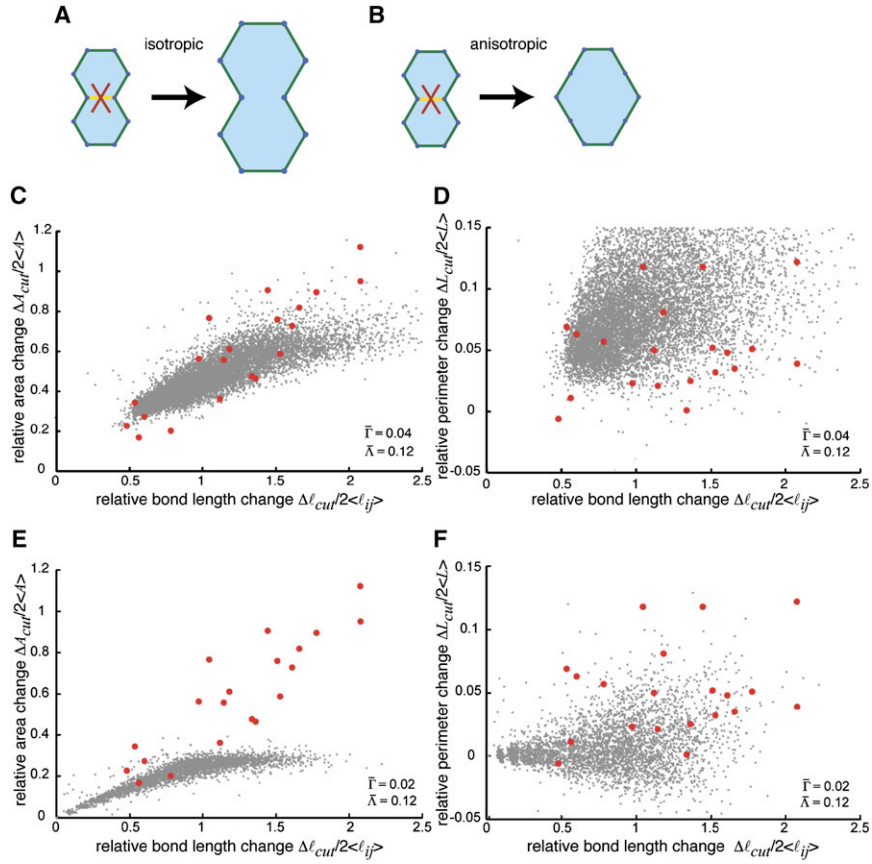

Figure 5. Anisotropic Displacements after Laser Ablation

(A and B) Schematic representation of cell-shape changes upon ablation of a cell boundary. The yellow line indicates cut boundary, and the red cross indicates cut site. (A) shows that isotropic deformation near the cut bond leads both to an increase of the combined perimeter L_{cut} (green outline) and of the combined area A_{cut} (blue) of adjacent cells. As shown in (B), for a strongly anisotropic deformation, the area changes significantly, whereas the perimeter can remain unchanged.

(C and E) Changes in the combined areas ΔA_{cut} of cells adjacent to an ablated bond, relative to twice the average cell area $\langle A \rangle$, are plotted as a function of the relative increase in the distance between the vertices of the cut bond $\Delta \ell_{cut}/2\langle \ell_{ij} \rangle$.

(D and F) Relative change of the perimeter $\Delta L_{cut}/2\langle L \rangle$ of the cells adjacent to the cut bond; $\langle L \rangle$ is the average cell perimeter. In (C)–(F), red dots show results from 20 experiments, and gray dots show the results of simulations with different parameter values for laser ablation (indicated).

which includes those of case I, is consistent with the observed movements.

Taken together, our comparison of experiment and theory has allowed us to restrict the range of possible parameter values to a small region corresponding to the intersection of the red, green, and blue outlined regions in Figure 3. With parameter values in this region, the vertex model accounts for the observed vertex movements induced by laser ablation, the epithelial packing geometries, and area variations observed in the *Drosophila* wing disc. The distribution of neighbor numbers does depend on physical parameters, but there is an extended region that is consistent with experiments. Area variability constrains parameter values more. Laser-ablation experiments constrain parameter values the most (Figure 3).

Some cells in proliferating wild-type disc epithelia normally undergo extrusion and apoptosis—the cause of cell elimination under wild-type conditions is not understood. Furthermore, cells that differ from their neighbors in signaling capacity [22, 23], growth rate [24, 25], or cytoskeletal organization [26] are extruded from the epithelium, even when cell death is prevented. During simulated proliferation with parameters consistent with packing geometry and laser ablation, the rate of T2 transitions is 12 per 100 cell divisions—similar to our estimate of the rate of cell elimination in vivo. This raises the possibility that cell extrusion is a consequence, at least in part, of the biophysical properties of cells and forces balances in the junctional network.

In the wing, the fact that clones of cells do not disperse [27, 28] has long suggested that few rearrangements occur during proliferation. In simulations of case I, few T1 transitions occur as the network grows (37/100 cell divisions), and clones remain cohesive. In contrast, in the case of a liquid-like tissue (case III), 146 T1 transitions occur per 100 cell divisions (Movies S7 and S8), and clones are invaded by unrelated cells. This suggests that the tendency for clones to remain contiguous during proliferation is a consequence of physical cellular properties.

In the future, our model might be extended to other problems in epithelial development, those such as asymmetric growth and hexagonal repacking. In this work, we have assigned each cell boundary the same line tension; however, this might be an oversimplification [9]. Future work could allow us to assess effects

of nonuniform cell-boundary line tension on directional growth. Furthermore, the present model already suggests a mechanism for the hexagonal repacking of the wing epithelium occurring during pupal stages. The disordered geometry of the proliferating wing epithelium represents a local minimum of the energy function. Because the global minimum in case I is a perfect hexagonal lattice, the energy function would bias fluctuations to bring the initially irregular network closer to the hexagonal ground state. Thus, annealing might be effective for remodeling the larval wing epithelial cells into a more hexagonal array. Simulations show that introducing fluctuations in line tension (which could correspond to fluctuations in adhesion and contractility) are sufficient to drive remodeling (Movie S6). However, remodeling in vivo is more complex. Hexagonal repacking requires the planar cell polarity proteins, which become polarized as repacking proceeds [9]. Although boundary-length fluctuations probably make an important contribution to repacking, any realistic description of this process must include the role of PCP proteins. Careful observation of fluctuation dynamics in both wild-type and PCP mutant wings will help us to extend our work to describe hexagonal repacking.

Supplemental Data

Experimental Procedures, eight figures, three tables, and eight movies are available at http://www.current-biology.com/cgi/content/full/17/24/2095/DC1/.

Acknowledgments

We gratefully acknowledge Tony Hyman, Henrik Bringman, and Stefan Grill for setting up the laser-ablation system and assisting us in its use. We thank Karsten Kruse for helpful discussions and Stefan Grill, Christian Dahmann, and Elisabeth Knust for critical comments on the manuscript. This work was supported by the Max-Planck Gesellschaft and by a grant to S.E. from the Deutsche Forschungsgemeinschaft (SPP 1111, Cell Polarity). J.R. was supported by a predoctoral fellowship of the Boehringer Ingelheim Fonds. B.A. is funded by Fondation pour la Recherche Médicale.

Received: August 3, 2007
Revised: October 19, 2007
Accepted: November 9, 2007
Published online: December 13, 2007

References

1. Chuai, M., Zeng, W., Yang, X., Boychenko, V., Glazier, J.A., and Weijer, C.J. (2006). Cell movement during chick primitive streak formation. Dev. Biol. *296*, 137–149.
2. Cui, C., Yang, X., Chuai, M., Glazier, J.A., and Weijer, C.J. (2005). Analysis of tissue flow patterns during primitive streak formation in the chick embryo. Dev. Biol. *284*, 37–47.
3. Bertet, C., Sulak, L., and Lecuit, T. (2004). Myosin-dependent junction remodelling controls planar cell intercalation and axis elongation. Nature *429*, 667–671.
4. Blankenship, J.T., Backovic, S.T., Sanny, J.S., Weitz, O., and Zallen, J.A. (2006). Multicellular rosette formation links planar cell polarity to tissue morphogenesis. Dev. Cell *11*, 459–470.
5. Fristrom, D. (1976). The mechanism of evagination of imaginal discs of Drosophila melanogaster. III. Evidence for cell rearrangement. Dev. Biol. *54*, 163–171.
6. Koppen, M., Fernandez, B.G., Carvalho, L., Jacinto, A., and Heisenberg, C.P. (2006). Coordinated cell-shape changes control epithelial movement in zebrafish and Drosophila. Development *133*, 2671–2681.
7. Tardieu, A. (1988). Eye lens proteins and transparency: From light transmission theory to solution X-ray structural analysis. Annu. Rev. Biophys. Biophys. Chem. *17*, 47–70.
8. Wootton, R. (1992). Functional morphology of insect wings. Annu. Rev. Entomol. *37*, 113–140.
9. Classen, A., Anderson, K., Marois, E., and Eaton, S. (2005). Hexagonal packing of *Drosophila* wing epithelial cells by the planar cell polarity pathway. Dev. Cell *9*, 805–817.
10. Otani, T., Ichii, T., Aono, S., and Takeichi, M. (2006). Cdc42 GEF Tuba regulates the junctional configuration of simple epithelial cells. J. Cell Biol. *175*, 135–146.
11. Franke, J.D., Montague, R.A., and Kiehart, D.P. (2005). Nonmuscle myosin II generates forces that transmit tension and drive contraction in multiple tissues during dorsal closure. Curr. Biol. *15*, 2208–2221.
12. Lewis, F.T. (1928). The correlation between cell division and the shapes and sizes of prismatic cells in the epidermis of cucumis. Anat. Rec. *38*, 341–376.
13. Gibson, M.C., Patel, A.B., Nagpal, R., and Perrimon, N. (2006). The emergence of geometric order in proliferating metazoan epithelia. Nature *442*, 1038–1041.
14. Graner, F., and Glazier, J.A. (1992). Simulation of biological cell sorting using a two-dimensional exended Potts model. Phys. Rev. Lett. *69*, 2013–2016.
15. Mombach, J., de Almeida, R., and Iglesias, J. (1993). Mitosis and growth in biological tissues. Phys. Rev. E Stat. Phys. Plasmas Fluids Relat. Interdiscip. Topics *48*, 598–602.
16. Hufnagel, L., Teleman, A.A., Rouault, H., Cohen, S.M., and Shraiman, B.I. (2007). On the mechanism of wing size determination in fly development. Proc. Natl. Acad. Sci. USA *104*, 3835–3840.
17. Stavans, J. (1993). The evolution of cellular structures. Rep. Prog. Phys. *56*, 733–789.
18. Narumiya, S., Ishizaki, T., and Uehata, M. (2000). Use and properties of ROCK-specific inhibitor Y-27632. Methods Enzymol. *325*, 273–284.
19. Winter, C.G., Wang, B., Ballew, A., Royou, A., Karess, R., Axelrod, J.D., and Luo, L. (2001). Drosophila Rho-associated kinase (Drok) links Frizzled-mediated planar cell polarity signaling to the actin cytoskeleton. Cell *105*, 81–91.
20. Zallen, J.A., and Wieschaus, E. (2004). Patterned gene expression directs bipolar planar polarity in *Drosophila*. Dev. Cell *6*, 343–355.
21. Rivier, N., and Lissowski, A. (1982). On the correlation between sizes and shapes of cells in epithelial mosaics. Journal of Physics A: Mathematical and General *15*, L143–L148.
22. Shen, J., and Dahmann, C. (2005). Extrusion of cells with inappropriate Dpp signaling from Drosophila wing disc epithelia. Science *307*, 1789–1790.
23. Gibson, M.C., and Perrimon, N. (2005). Extrusion and death of DPP/BMP-compromised epithelial cells in the developing Drosophila wing. Science *307*, 1785–1789.
24. de la Cova, C., Abril, M., Bellosta, P., Gallant, P., and Johnston, L.A. (2004). Drosophila myc regulates organ size by inducing cell competition. Cell *117*, 107–116.
25. Moreno, E., and Basler, K. (2004). dMyc transforms cells into super-competitors. Cell *117*, 117–129.
26. Janody, F., and Treisman, J.E. (2006). Actin capping protein alpha maintains vestigial-expressing cells within the Drosophila wing disc epithelium. Development *133*, 3349–3357.
27. Garcia-Bellido, A., Ripoll, P., and Morata, G. (1973). Developmental compartmentalisation of the wing disk of Drosophila. Nat. New Biol. *245*, 251–253.
28. Garcia-Bellido, A., Ripoll, P., and Morata, G. (1976). Developmental compartmentalization in the dorsal mesothoracic disc of Drosophila. Dev. Biol. *48*, 132–147.